Ambipolar-transporting coaxial nanotubes with a tailored molecular graphene–fullerene heterojunction

Yohei Yamamoto[a,1], Guanxin Zhang[a,1], Wusong Jin[a], Takanori Fukushima[b,c,2], Noriyuki Ishii[d], Akinori Saeki[e], Shu Seki[e], Seiichi Tagawa[e], Takeo Minari[f], Kazuhito Tsukagoshi[f], and Takuzo Aida[a,c,2]

[a]Nanospace Project, Exploratory Research for Advanced Technology–Solution Oriented Research for Science and Technology, Japan Science and Technology Agency, National Museum of Emerging Science and Innovation, 2-41 Aomi, Koto-ku, Tokyo 135-0064, Japan; [b]Functional Soft Matter Engineering Laboratory, Advanced Science Institute, RIKEN, 2-1 Hirosawa, Wako, Saitama 351-0198, Japan; [c]Department of Chemistry and Biotechnology, School of Engineering, and Center for NanoBio Integration, University of Tokyo, 7-3-1 Hongo, Bunkyo-ku, Tokyo 113-8656, Japan; [d]Institute for Biological Resources and Functions, National Institute of Advanced Industrial Science and Technology, Tsukuba Central-6, 1-1-1 Higashi, Tsukuba, Ibaraki 305-8566, Japan; [e]Institute of Scientific and Industrial Research, Osaka University, 8-1 Mihogaoka, Ibaraki, Osaka 567-0047, Japan; and [f]International Center for Materials and Nanoarchitectonics, National Institute for Materials Science, 1-1 Namiki, Tsukuba, Ibaraki 305-0044, Japan

Edited by Timothy M. Swager, Massachusetts Institute of Technology, Cambridge, MA, and approved October 19, 2009 (received for review May 21, 2009)

Despite a large steric bulk of C_{60}, a molecular graphene with a covalently linked C_{60} pendant [hexabenzocoronene (HBC)–C_{60}; 1] self-assembles into a coaxial nanotube whose wall consists of a graphite-like π-stacked HBC array, whereas the nanotube surface is fully covered by a molecular layer of clustering C_{60}. Because of this explicit coaxial configuration, the nanotube exhibits an ambipolar character in the field-effect transistor output [hole mobility (μ_h) = 9.7×10^{-7} cm^2 V^{-1} s^{-1}; electron mobility (μ_e) = 1.1×10^{-5} cm^2 V^{-1} s^{-1}] and displays a photovoltaic response upon light illumination. Successful coassembly of 1 and an HBC derivative without C_{60} (2) allows for tailoring the p/n heterojunction in the nanotube, so that its ambipolar carrier transport property can be optimized for enhancing the open-circuit voltage in the photovoltaic output. As evaluated by an electrodeless method called flash-photolysis time-resolved microwave conductivity technique, the intratubular hole mobility (2.0 cm^2 V^{-1} s^{-1}) of a coassembled nanotube containing 10 mol % of HBC–C_{60} (1) is as large as the intersheet mobility in graphite. The homotropic nanotube of 2 blended with a soluble C_{60} derivative [(6,6)-phenyl C_{61} butyric acid methyl ester] displayed a photovoltaic response with a much different composition dependency, where the largest open-circuit voltage attained was obviously lower than that realized by the coassembly of 1 and 2.

ambipolar transport | field-effect transistor | nanotube | photovoltaic | self-assembly

For addressing the imminent issue of energy, one of the principal subjects is to develop solar cells that are capable of efficiently converting light energy into electrical outputs. Although silicon-based solar cells have been commercialized, there exists a strong demand for organic solar cells because organic materials are flexible and easy to process (1). An ideal configuration for organic photovoltaics (PVs) consists of properly connected hole- and electron-transporting layers (p/n heterojunction) formed from electron-donating (D) and electron-accepting (A) molecular components, respectively, with neither charge–transfer complexation nor macroscopic D/A segregation (2–4). For the last decade, a major progress has been made by the "bulk heterojunction" approach (5–9), which integrates, in most cases, electron-accepting molecules such as fullerenes into hole-transporting media composed of π-conjugated polymers. However, despite the practical importance of this approach, the interface for the resulting p and n domains is, in principle, hard to tailor at the molecular level. As a new strategy to solve this essential problem, molecular assembly of covalently or noncovalently connected D–A modules has attracted increasing attention (10). In 2004, Würthner et al. (11) reported that self-assembly of a hydrogen-bonded D–A–D triad consisting of oligo(*p*-phenylene vinylene) (D) and perylenediimide (A) affords photoconductive nanofibers. To realize selective formation of bicontinuous D/A arrays in bulk, an amphiphilic oligothiophene–C_{60} covalent D–A dyad with a liquid crystalline character has been developed (12). Dye-sensitized wet solar cells have been prepared by a modification of electrodes through layer-by-layer assembly of oligo(*p*-phenylene)/naphthalenediimide (13) and porphyrin/C_{60} (14), designed to form a heterojunction. Despite these pioneering examples, rational design of molecularly engineered D/A heterojunctions, leading to PV outputs, remains a big challenge.

In 2006, we reported that a hexa-*peri*-hexabenzocoronene (HBC)–trinitrofluorenone (TNF) covalent D–A dyad self-assembles into a photoconductive coaxial nanotube, where a TNF molecular layer laminates a graphite-like bilayer composed of π-stacked HBC units (15). HBC, a small fragment of graphene, is a basic structural element for graphite and carbon nanotubes. Pioneering works by Müllen and coworkers (16, 17) made it possible to use such a large, polycyclic aromatic hydrocarbon for organic electronics. Our TNF-appended nanotube was intended for PV. However, in a preliminary study using a field-effect transistor (FET) device, this nanotube did not show any sign of electron transport originating from the TNF layer on the tube surface, but only a hole-transport property due to the π-stacked HBC array. Therefore, we turned to focus on C_{60}, which is widely used as an electron-transporting component for organic PV devices (1–3, 6–9). In this article, we report an "all-in-one" PV nanotube via controlled self-assembly of an HBC–C_{60} covalent D–A dyad (**1**; Fig. 1*A*; see *SI Text* and Fig. S1). This nanotube is a highly carbon-rich assembly adopting a coaxial D/A heterojunction (Fig. 1 *B* and *C*) and can be regarded as a low-dimensional hybrid of a "molecular graphite" and a quasi-zero-dimensional nanocarbon.

Our recent systematic study on the self-assembly of Gemini-shaped HBC amphiphile **2** (Fig. 1*A*) and its derivatives revealed that the long, paraffinic side chains and two phenylene units, along with the large π-conjugated HBC core, are the essential structural elements for nanotubular assembly (18–20). This observation, in turn, suggests that the triethylene glycol (TEG) chains, which are not essential for the controlled assembly, may be used as a scaffold for anchoring functional groups onto the nanotube surface. In fact, various nanotubes with different

Author contributions: Y.Y., T.F., and T.A. designed research; Y.Y., G.Z., W.J., N.I., and A.S. performed research; Y.Y., A.S., S.S., S.T., T.M., and K.T. analyzed data; and Y.Y., T.F., and T.A. wrote the paper.

The authors declare no conflict of interest.

This article is a PNAS Direct Submission.

[1]Y.Y. and G.Z. contributed equally to this work.

[2]To whom correspondence may be addressed. E-mail: fukushima@riken.jp or aida@macro.t.u-tokyo.ac.jp.

This article contains supporting information online at www.pnas.org/cgi/content/full/0905655106/DCSupplemental.

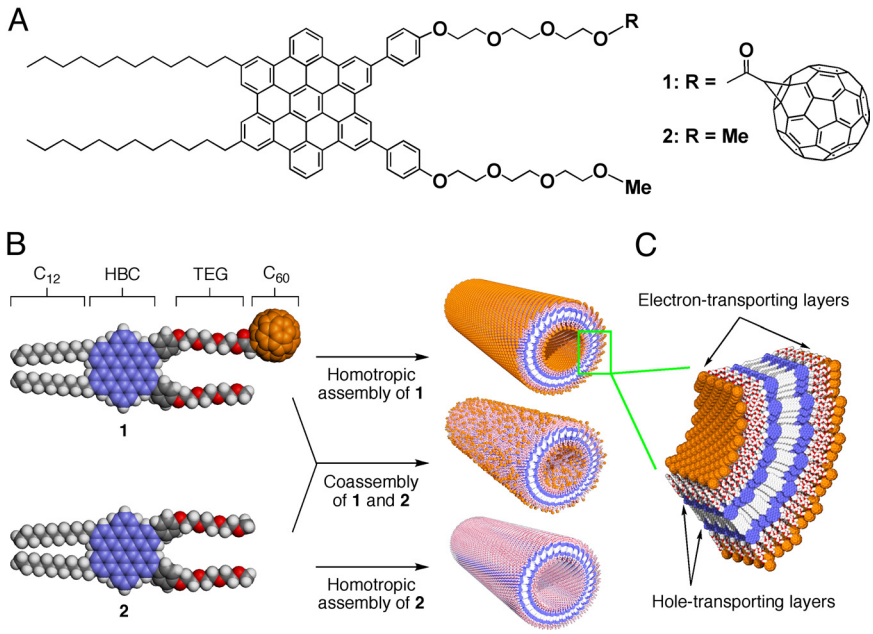

Fig. 1. Schematic representations of Gemini-shaped HBC derivatives and their nanotubes. (*A*) Molecular structures of HBC–C_{60} dyad **1** and HBC **2**. (*B*) Schematic representation of the formation of homotropic and coassembled nanotubes of **1** and **2**. (*C*) Schematic representation of the wall structure of the nanotube of **1**, where an electron-transporting molecular layer of clustering C_{60} (orange) laminates a hole-transporting, graphite-like layer of π-stacked HBC units (blue).

surface groups have successfully been obtained from HBC amphiphiles carrying functional groups at the TEG termini. Examples include HBC nanotubes appended with small surface pendants, such as allyl (21), thioacetate (22), and azide (23), or relatively large but planar pendants, such as coumarine (24), TNF (15, 25), and isothiouronium ion (26). Among these successful examples, self-assembly of an HBC amphiphile carrying spatially demanding norbornene pendants exceptionally gave a coiled nanostructure, a sterically relaxed form of the tubular assembly (27, 28). This result suggests that norbornene might be the upper limit in steric bulk for the exclusive formation of nanotubes. Because C_{60} is much bulkier than norbornene and tends to aggregate, we were initially afraid that the nanotube formation from HBC–C_{60} (**1**) might not take place. However, to our surprise, **1** successfully self-assembled into a perfect coaxial nanotubular structure, whose C_{60} and graphite-like layers allowed for an ambipolar charge-carrier transport. Being encouraged by successful examples using some other HBC amphiphiles (19, 25, 27, 28), we also attempted coassembly of **1** and HBC **2** without C_{60}. Consequently, the hole and electron mobilities in the nanotube could be properly optimized for enhancing the open-circuit voltage in the PV output.

Results and Discussion

Coaxial Nanotubes by Self-Assembly and Coassembly. HBC–C_{60} covalent dyad **1** was synthesized by esterification of the hydroxyl group of HBC **4** with metano[60]fullerene carboxylic acid **5** (*SI Text* and Fig. S2). As a typical procedure for the self-assembly, a toluene suspension of **1** (0.2 mM) was ultrasonicated for 1 h and heated at 100 °C. The resultant orange-colored solution was allowed to cool to 25 °C and aged for a few hours, affording a brown-colored suspension. Scanning electron microscopy (SEM) of an air-dried suspension exclusively showed cylindrical nanowires with an open-ended hollow structure (Fig. 2*A*). As confirmed by transmission electron microscopy (TEM), these nanotubes were uniform in diameter (22 nm) and wall thickness

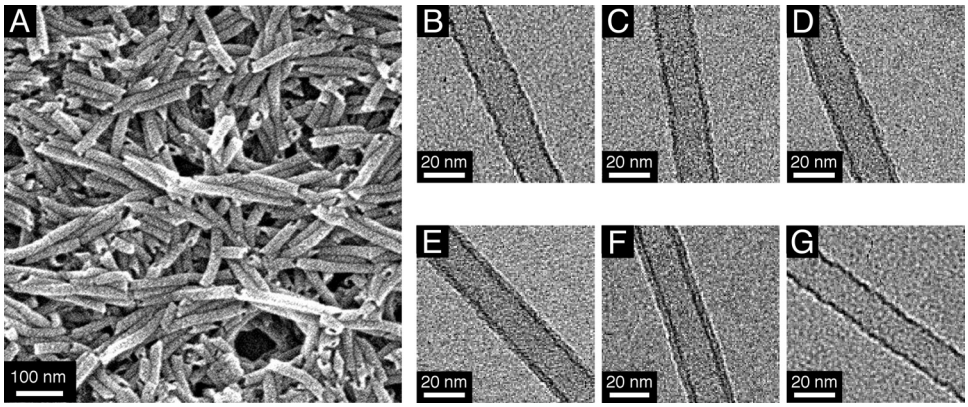

Fig. 2. Electron micrographs of the homotropic and coassembled nanotubes of **1** and **2**. (*A*) SEM micrograph of an air-dried toluene suspension of the homotropic nanotube of **1**. (*B–F*) TEM micrographs of air-dried toluene suspensions of the homotropic nanotubes of **1** (*F*) and **2** (*B*), and coassembled nanotubes with f_1 = 25% (*C*), 50% (*D*), and 75% (*E*). (*G*) TEM micrograph of an air-dried MeOH suspension of the nanotube of **1** after hydrolysis of the ester groups.

(4.5 nm; Fig. 2*F*). Electronic absorption spectroscopy of the suspension displayed two red-shifted absorption bands at 425 and 458 nm, along with a broad band at 330–365 nm (Fig. S3*A*), which are commonly observed for tubularly assembled HBC derivatives (20). Infrared spectroscopy showed CH_2 stretching vibrations at 2,917 (ν_{anti}) and 2,848 (ν_{sym}) cm^{-1} (Fig. S3*B*), suggesting that the dodecyl side chains of **1** are stretched to form a bilayer tape via interdigitation (20). Powder x-ray diffraction of the nanotube of **1** exhibited a diffraction peak with a *d* spacing of 3.47 Å (2θ = 25.7°; Fig. S3*C*), which is assignable to the plane-to-plane separation of the π-stacked HBC units (20).

To verify whether the HBC nanotube of **1** is indeed covered by a molecular layer of clustering C_{60} pendants, a brown-colored toluene suspension of the nanotubes was poured into methanolic KOH, and the resulting mixture was gently stirred at 25 °C (*SI Text*). After 48 h, an yellow-colored dispersion resulted, whose mass spectrometry displayed only a molecular ion peak (m/z = 1,320.95) due to HBC **4** (Fig. S2), indicating the occurrence of a hydrolytic cleavage of the ester linkage of **1** (Fig. S4*A*). As confirmed by TEM, the assembly still preserved a tubular morphology (Fig. 2*G*). Noteworthy, dark-colored thin regions, observed on the inner and outer surfaces of the original nanotube (Fig. 2*F*), were no longer present after the ester hydrolysis. The wall thickness (3 nm) and diameter (20 nm) of the resulting nanotube were identical to those obtained by self-assembly of **2** (Fig. 2*B*). Because of an enhanced hydrophilic nature of the surface, the nanotubes after the removal of the C_{60} pendants were completely dispersed in MeOH (Fig. S4 *B* and *C*). Meanwhile, attempted self-assembly of HBC **4** did not result in the formation of a nanotubular structure, but an ill-defined agglomerate.

Although C_{60} has a large steric bulk, much greater than norbornene (27, 28), C_{60}-appended **1** self-assembles into a nanotubular structure exclusively (*vide ante*). Considering a strong tendency for C_{60} to form a cluster, we wondered whether the assembly of **1** might be affected by such an attractive interaction of the C_{60} pendants. Along with this fundamental question, a strong demand from PV for tuning the hole and electron mobilities (*vide infra*) prompted us to investigate whether **1** and **2** may coassemble or just self-assemble independently from one another. Thus, **1** and **2** were mixed in toluene at seven different molar ratios, with the mole fraction of **1** (f_1) ranging from 10% to 90% [(**1** + **2**) = 0.2 mM], and the resulting suspensions were subjected to the assembling conditions established for the homotropic nanotubular assembly of **1**. As shown in Fig. S5, SEM and TEM microscopy allowed us to confirm exclusive formation of nanotubes at any molar ratios of **1** to **2**. By reference to the homotropic nanotube of **1** (Fig. 2*F*), an enlarged TEM micrograph of the nanotube, obtained from a 1:1 mixture of **1** and **2** (f_1 = 50%; Fig. 2*D*), showed that the dark-colored thin region on the nanotube surface, due to the clustering C_{60} pendants, is fragmentary. The same was true for the nanotubes with f_1 = 25% and f_1 = 75% (Fig. 2 *C* and *E*, respectively), where the continuity of the dark-colored thin region was much better in the latter nanotube than the former. To confirm whether these observations can be ascribed to the coassembly of **1** and **2**, we investigated fluorescence-quenching characteristics of the nanotubes. The energy diagrams of the HBC and C_{60} units (*SI Text* and Fig. S1) suggest that they can communicate with one another by electron transfer upon photoexcitation. Even when the TEG spacers adopt an extended conformation, the HBC and C_{60} layers in the tubular wall are supposed to locate within an electron-transferrable distance (≈1 nm). Therefore, the C_{60} pendants could efficiently quench the fluorescence of HBC, particularly when HBC **2** is coassembled with **1**. In fact, not only the homotropic nanotube of **1** but also the nanotubes obtained from the mixtures of **1** and **2** displayed complete fluorescence quenching when the mole fraction of **1** (f_1) in the coassembling mixture was higher than 25% (Fig. S6). Even when f_1 was decreased to 10%, the degree of fluorescence-quenching remained very high (93%). In contrast, photoexcitation

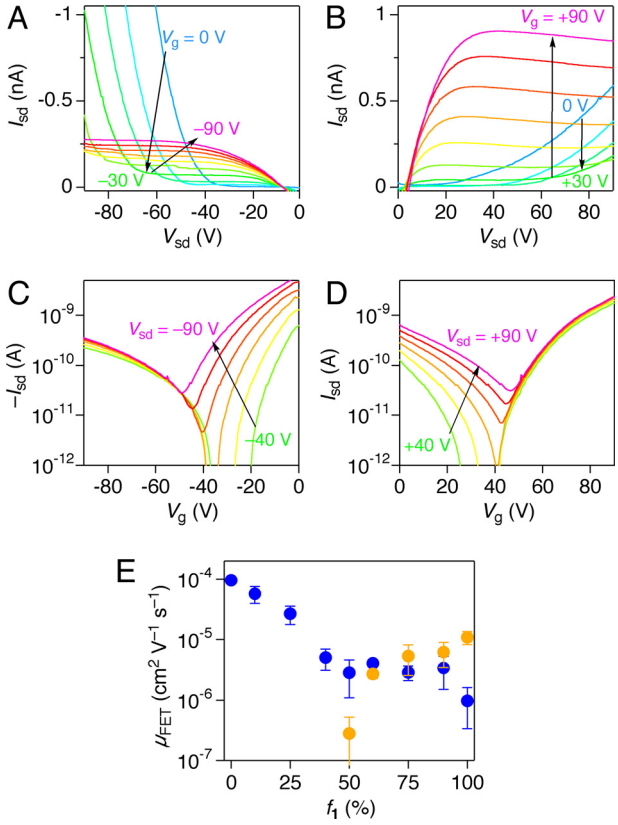

Fig. 3. FET properties of the homotropic and coassembled nanotubes of **1** and **2**. (*A* and *B*) Output characteristics of a cast film of the nanotube of **1** for negative (*A*) and positive (*B*) gate voltages (V_g). (*C* and *D*) Transfer characteristics of a cast film of the nanotube of **1** for negative (*C*) and positive (*D*) source–drain voltages (V_{sd}). (*E*) Plots of the field-effect mobilities (μ_{FET}) of electron (orange) and hole (blue) versus f_1.

of a mixture of the homotropic nanotubes of **1** and **2** with f_1 = 10% resulted in only 43% quenching of the HBC fluorescence (Fig. S6). The TEM and photochemical observations described above strongly indicate that **1** and **2** coassemble into a single nanotubular structure. Thus, the fragmentary, dark-colored thin regions, observed in the TEM micrographs of the coassembled nanotubes (Fig. 2 *C–E*), suggest that C_{60}-appended **1** is not dispersed uniformly but localized to form domains, probably because of an attractive force operative among the C_{60} pendants.

Ambipolar Carrier Transport Properties. The nanotube of **1** adopts a coaxial configuration in such a way that the graphite-like π-stacked HBC layer is laminated on its both sides by a molecular layer of clustering C_{60} pendants. In general, HBC assemblies act as hole conductors (17, 18, 29), whereas a cluster of C_{60} is known to provide an electron-transport pathway (30). By means of an FET device setup, we confirmed that the nanotube of **1** actually behaves as both p- and n-type conductors. Furthermore, these conduction profiles coincided well with the morphological features of the (co)assembled nanotubes (Fig. 2 *B–F*). As a typical experiment, a toluene suspension of the nanotube of **1** was cast onto a 1,1,1,3,3,3-hexamethyldisilazane (HMDS)-treated SiO_2 (200 nm)/Si substrate, on which Au was then thermally deposited to form source and drain electrodes (*SI Text*). In the output characteristics (Fig. 3 *A* and *B*), the superlinear source–drain current (I_{sd}) was gradually suppressed as the gate bias voltage (V_g) was increased both toward the positive and negative sides. At higher V_g, I_{sd} increased in proportion to an increment of the applied source–drain voltage

(V_{sd}) and then leveled off. Furthermore, the transfer curves displayed *V*-shape profiles (Fig. 3 *C* and *D*). These behaviors are typical of ambipolar FET (31). From the saturated regions in the transfer curves, the electron (μ_e) and hole (μ_h) mobilities of the nanotube of **1** were evaluated as 1.1×10^{-5} and 9.7×10^{-7} cm^2 V^{-1} s^{-1}, respectively (*SI Text*).

A detailed study of the coassembled nanotubes revealed that both μ_e and μ_h are dependent nonlinearly on the nanotube composition (Fig. 3*E*). For example, μ_e decreased gradually as f_1 was decreased from 100% to 60%, and then it fell off abruptly thereafter. In particular, no electron mobility was detected when f_1 was lower than 40%, suggesting that the C_{60} cluster on the nanotube surface, as visualized by TEM (Fig. 2 *B–F*), completely loses an effective continuity for long-range electron transport. On the other hand, a cast film of the nanotube of **2** without C_{60} exhibited only a p-type FET property, where μ_h of 1.0×10^{-4} cm^2 V^{-1} s^{-1}, thus obtained, is two orders of magnitude greater than that observed for the homotropic nanotube of **1**. Nevertheless, only a small increase in f_1 from 0 to 25% resulted in a considerable decrease in μ_h (80%). For such a complicated composition dependency of μ_h, we consider that the molecular layer of clustering C_{60} may prevent hole injection into the graphite-like inner layer from the source electrode. In addition to this, a large steric bulk of C_{60} may certainly hamper ideal π-stacking of the HBC units (25).

Intratubular Carrier Transport Properties. For evaluating the intratubular carrier transport properties, we used a flash-photolysis time-resolved microwave conductivity (FP-TRMC) technique (see *Methods* and ref. 32), which allows for probing the motion of photocarriers under a rapidly oscillating electric field. Because of this probing function, the FP-TRMC technique does not require electrodes for charge injection, so that one can evaluate intrinsic dynamics of mobile carriers. Furthermore, under such high-resonant frequency conditions, charge carriers can migrate only in a nanoscale range (33). Therefore, FP-TRMC profiles of the nanotubes are considered to reflect mostly the intratubular carrier transport events.

Upon laser flash, rise and decay profiles of a TRMC signal, given by $\phi\Sigma\mu$, are observed, where ϕ and $\Sigma\mu$ represent photocarrier generation yield and sum of the mobilities of generated charge carriers, respectively. In general, the maximum value of $\phi\Sigma\mu$ ($\phi\Sigma\mu_{max}$) is used for evaluating the photoconductivity of a material. As reported previously, the homotropic nanotube of **2** without C_{60}, upon laser excitation at 355 nm, shows only a small value of $\phi\Sigma\mu_{max}$ (25). However, as shown in Fig. 4*A* (transient profiles of $\phi\Sigma\mu$; Fig. S7*A*), $\phi\Sigma\mu_{max}$ was progressively enhanced upon increase of the content of **1** and furnished at $f_1 = 25\%$ maximum value, which is roughly 50-fold greater than that of the homotropic nanotube of **2**. $\phi\Sigma\mu_{max}$ then gradually decreased as f_1 was further increased, possibly because of a decrease in the hole mobility through the π-stacked HBC array. This tendency coincides with the composition-dependent profile of μ_h in the FET output, discussed in the above section (Fig. 3*E*). For evaluating the intratubular carrier mobility of the nanotube from $\phi\Sigma\mu_{max}$, photogenerated charge carriers have to be quantified. However, among the nanotubes tested for FP-TRMC, only the coassembled nanotube with $f_1 = 10\%$ gave a transparent cast film suitable for transient absorption spectroscopy (TAS) to quantify the photocarriers. Upon exposure of this cast film to a 355-nm laser light, an absorption band assignable to an HBC radical cation ($HBC^{\cdot+}$) appeared at 605 nm, along with bleaching of the absorption bands of HBC at 430 and 465 nm (Fig. 4*B*). The decay profile of the transient absorption at 605 nm agreed well with that of the transient conductivity observed by FP-TRMC (Fig. 4*C*). Thus, the carrier mobility of the nanotube was evaluated as 1.4–2.0 cm^2 V^{-1} s^{-1} (Fig. 4*D*; see also *Methods*), which is greater than those reported for HBC-based discotic liquid crystals (34) and even close to the intersheet mobility in graphite (≈3 cm^2 V^{-1} s^{-1}) (35).

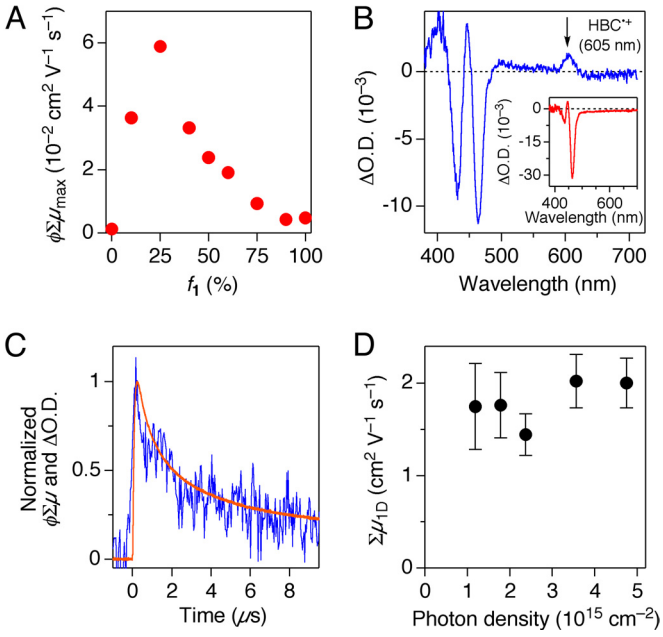

Fig. 4. Transient conductivity and absorption profiles of the homotropic and coassembled nanotubes of **1** and **2**. (*A*) Plots of $\phi\Sigma\mu_{max}$ versus f_1. Transient conductivity ($\phi\Sigma\mu$) in FP-TRMC is given by multiplication of photocarrier generation yield (ϕ) and sum of charge carrier mobilities ($\Sigma\mu$) (32). (*B*) FP-TAS at 25 °C of a cast film of the coassembled nanotube with $f_1 = 10\%$ upon photoirradiation at 355 nm (photon density, 3.6×10^{15} cm^{-2}). (*Inset*) FP-TAS at 25 °C of a cast film of the homotropic nanotube of **2**. Transient species arising from C_{60} were not observed because of a detection limit of the spectroscope. (*C*) Normalized FP-TRMC (orange) and FP-TAS (blue; $\lambda = 605$ nm) profiles of a cast film of the coassembled nanotube with $f_1 = 10\%$, upon photoirradiation at 355 nm (photon density, 1.2×10^{15} cm^{-2}). (*D*) Plots of $\Sigma\mu_{1D}$ for a cast film of the coassembled nanotube with $f_1 = 10\%$ versus photon density.

PV Device Performances. As already described, only a small content of C_{60}-appended **1** in the coassembled nanotube gives rise to a very efficient quenching of the HBC fluorescence (Fig. S6). This fact indicates that the probability of HBC-to-C_{60} electron transfer is enhanced by a rapid migration of the excitation energy along the π-stacked HBC array (25). Having this positive sign in mind, we evaluated PV properties of the nanotubes. Because none of the nanotubes, upon drop casting, could form pinhole-free thin films, which are necessary for the conventional top-contact PV cell, we designed a dedicated device with a side-direction channel (Fig. 5*A*), which may be generally applicable to fiber samples. Thus, a toluene suspension of the nanotube of C_{60}-appended **1** was cast onto a fluoroalkyl-coated glass substrate, prepatterned with PEDOT:PSS/Au/Ti [PEDOT, poly(3,4-ethylenedioxythiophene); PSS, poly(styrenesulfonate)] and TiO_x/Ti/Al electrodes with an 8- to 15-μm separation (*SI Text* and Fig. S8*A*). Upon exposure to light of wavelength λ = 300–650 nm from the backside of the glass substrate, the cast film displayed a PV response with an open-circuit voltage (V_{OC}) of 0.46 V (Fig. 5*B*). The short-circuit current (I_{SC}) was enhanced in linear proportion to the light intensity (Fig. S8*B*) and switched promptly and repeatedly in response to turning on and off the light (light power density, 0.39 mW mm^{-2}; Fig. S8*C*). The on/off current ratio was nearly 10^3 (Fig. 5*B Inset*).

Likewise, PV devices were prepared from the coassembled nanotubes, and their performances were investigated (Fig. S8*D*). As shown in Fig. 5*C*, the V_{OC} value increased from 0.09 to 0.50

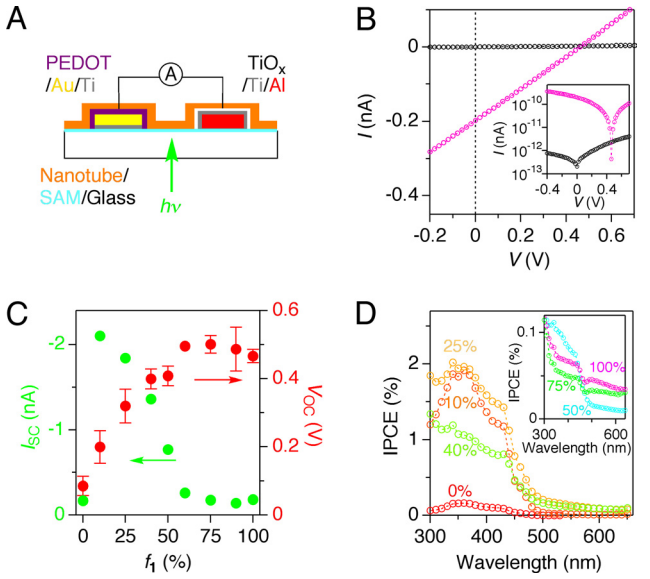

Fig. 5. PV performances of the homotropic and coassembled nanotubes of **1** and **2**. (*A*) Schematic illustration of the device configuration for PV measurements. (*B*) *I–V* profiles of a cast film of the nanotube of **1** in the dark (black) and upon photoirradiation (pink, λ = 300–650 nm, 0.39 mW mm^{-2}). (*Inset*) log *I–V* profiles of a cast film of the nanotube of **1** in the dark (black) and upon photoirradiation (pink). (*C*) Plots of V_{OC} (red) and I_{SC} (green) versus f_1. (*D*) IPCE spectra of cast films of the nanotubes with f_1 = 0%, 10%, 25%, and 40%. (*Inset*) IPCE spectra of cast films of the nanotubes with f_1 = 50%, 75%, and 100%.

V as f_1 was increased from 0 to 75%, and then slightly decreased to 0.46 V when f_1 reached 100%. Of particular importance, V_{OC} was maximized at a point where the hole and electron mobilities, as evaluated by FET, were well-balanced with one another (f_1 = 60–75%; Fig. 3*E*). On the other hand, among the nine tested samples, the coassembled nanotube with the lowest mole fraction of **1** (f_1 = 10%) displayed the largest I_{SC} (Fig. 5*C*). Here, one may wonder if the observed I_{SC} profile has a certain correlation with the intratubular conducting property ($\phi\Sigma\mu_{max}$; Fig. 4*A*). To address this interesting issue, not only $\phi\Sigma\mu_{max}$ but also the photocarrier lifetime ($\tau_{1/e}$) should be taken into account, because the PV outputs are steady-state photophysical properties. Thus, the $\phi\Sigma\mu_{max}$ values observed at different compositions were multiplied by the corresponding $\tau_{1/e}$ values (Fig. S7*B*). When the products ($\phi\Sigma\mu_{max} \times \tau_{1/e}$) were plotted against f_1, a maximum appeared at f_1 = 10% (Fig. S7*C*). This composition dependency agrees well with that of I_{SC} (Fig. 5*C*), indicating that the intratubular carrier transport property is a dominant factor to determine the photocurrent output of the PV device. Although the fill factor (FF) is low and hardly changed (0.25–0.30) with f_1 (Fig. S8*E*), the relative power conversion efficiency, given by $V_{OC} \times I_{SC} \times$ FF, was maximized at f_1 = ≈25% (Fig. S8*F*). Among the nanotubes with different compositions, that with f_1 = 25%, when excited at its absorption maximum (360 nm), also showed the largest incident photon-to-current conversion efficiency (IPCE ≈2%). Because the IPCE spectra of the cast films of the nanotubes were almost identical to their electronic absorption spectra (Fig. 5*D*), both HBC and C_{60} chromophores contribute to the photocurrent generation.

As a control, the homotropic nanotube of **2**, suspended in toluene, was mixed with a soluble fullerene, such as (6,6)-phenyl C_{61} butyric acid methyl ester (PCBM) at mole ratios [PCBM]/[**2**] of 0.25, 0.5, and 1.0 (corresponding to f_1 = 25%, 50%, and 100%, respectively). Cast films of the resulting blends showed a PV response (Fig. S9*A*), suggesting that the nanotubes are wrapped by PCBM without disruption, affording a p/n-heterojunction. When the mole fraction of PCBM was increased (Fig. S9*B*), I_{SC} gradually became larger and furnished 2 nA at [PCBM]/[**2**] = 1.0, which is comparable to that attained by the coassembled nanotube with f_1 = 10% (Fig. 5*C*). This observation casts a clear contrast between the covalently linked and blended D/A systems. Similarly to I_{SC}, V_{OC} became larger upon increment of the mole ratio [PCBM]/[**2**] from 0.25 to 1.0 (Fig. S9*B*). However, because of a marked saturation tendency, V_{OC} stayed only in a low range from 0.24 to 0.32 V and never surpassed the V_{OC} value of 0.5 V realized by the coassembled nanotube with f_1 = 75%. This observation indicates a clear advantage of our molecular design over D/A blending for tailoring the p/n heterojunction.

Conclusions

We have succeeded in designing the all-in-one PV nanotube by controlled assembly of a fullerene (C_{60})-appended molecular graphene **1** as a covalently connected D–A dyad. This highly carbon-rich discrete nanostructure is characterized by a coaxial configuration, where a hole-transporting, graphite-like layer is covered on both sides by an electron-transporting molecular layer of C_{60}. Because of such an explicit p/n heterojunction, the nanotube is photoconductive and displays an ambipolar character in the FET device output. By successful coassembly of **1** and **2** without C_{60}, tailoring of the p/n heterojunction in the nanotube is possible. Structural/electronic features of the nanotubes with different compositions and PV device outputs of their film samples were thoroughly investigated, using as references blend samples of the homotropic nanotube of **2** with a soluble C_{60}. Remarkable features include (*i*) a facilitated electron transfer by a rapid energy migration along the π-stacked HBC array, (*ii*) a large intratubular carrier mobility comparable to the intersheet mobility in graphite, and (*iii*) a clear correlation between the intratubular conductivity ($\phi\Sigma\mu_{max} \times \tau_{1/e}$) and current profile ($I_{SC}$) of the PV output. Even more important is that the open-circuit voltage of the PV output (V_{OC}), which strongly reflects the ambipolar character, can be enhanced by making a good balance between the hole and electron mobilities of the nanotube through coassembly. These findings are expected to contribute to the molecular-level understanding and advanced design of p/n heterojunction for organic PVs.

Methods

FP-TRMC, Fluorescence Spectroscopy, and FP-TAS. FP-TRMC, fluorescence spectra, and FP-TAS were measured with an identical geometry by using an in situ TRMC-TAS system (32). A resonant cavity was used to obtain a high degree of sensitivity in the conductivity measurements. The resonant frequency and microwave power were set at ≈9.1 GHz and 3 mW, respectively, so that the electric field of the microwave was small enough not to disturb the thermal motion of charge carriers. The charge carriers were photochemically generated by using the third-harmonic generation (355-nm) light pulses from a Spectra-Physics model GCR-130 Nd:YAG laser (5- to 8-ns pulse duration), with the incident photon densities ranging from 1.2 × 10^{15} to 4.8 × 10^{15} photons cm^{-2}. The TRMC signal, picked up by a diode (rise time <1 ns), was monitored by a Tektronics model TDS3052B digital oscilloscope. The observed conductivities were converted into normalized values, given by a photocarrier generation yield (ϕ) multiplied by the sum of the charge carrier mobilities ($\Sigma\mu$), according to an equation, $\phi\Sigma\mu = (1/eAI_0F_{light})(\Delta P_r/P_r)$, where, e, A, I_0, F_{light}, P_r, and ΔP_r denote unit charge of a single electron, sensitivity factor (S^{-1} cm), incident photon density of excitation laser (photon cm^{-2}), filling factor (cm^{-1}), and reflected microwave power and its change, respectively. In the fluorescence measurements, emission from a sample was guided into a Hamamatsu model C7700 wide-dynamic-range streak camera. Likewise, FP-TAS was measured by using continuous white light from a xenon lamp as a probe. All of the experiments were performed at 25 °C in air.

Nanosecond Electron-Beam Pulse-Radiolysis TAS. Nanosecond electron-beam pulse-radiolysis TAS (nsEB-PR-TAS) experiments were carried out to measure photoabsorption spectra and evaluate molar extinction coefficient (ε) of HBC^{+} by using a CH_2Cl_2 solution of **2** (0.2 mM) containing 20 mM biphenyl (Bp) as a hole mediator (Fig. S7 *D* and *E*). A 27-MeV electron beam with ≈8-ns

duration from the linac at the Institute of Scientific and Industrial Research, Osaka University, was used as an irradiation source (32). A xenon flash lamp was used as a probe light source. The nsEB-PR-TAS was measured by a Hamamatsu model PMA-11 optical multichannel analyzer. For kinetic studies, the white light was separated into spectrum components by a Ritsu model MC-10N monochromator and detected by a Hamamatsu model S1722 Si PIN photodiode. The signals were collected by a Tektronics model SCD1000 transient digitizer.

Determination of 1D Carrier Mobility. One-dimensional carrier mobility, $\Sigma\mu_{1D}$, was given by $2 \times \Sigma\mu_{max}$, because most nanotubes lay two-dimensionally on the substrates. $\Sigma\mu_{max}$ was determined by using the $\phi\Sigma\mu_{max}$ value in FP-TRMC divided by ϕ. The ϕ was given by the ratio of the number of photogenerated charge carriers (N_c) to that of absorbed photons, where N_c was estimated from ΔOD in FP-TAS of a cast film of the nanotube with $f_1 = 10\%$ (Fig. 4*B*) and ε of $HBC^{\bullet+}$ at 605 nm. The ε value of $HBC^{\bullet+}$ was determined as $1.0 \times 10^4\ M^{-1}\ cm^{-1}$ by the nsEB-PR-TAS experiments (Fig. S7*F*).

1. Brabec C, Scherf U, Dyakonov V, eds (2008) *Organic Photovoltaics: Materials, Device Physics, and Manufacturing Technologies* (Wiley-VCH, Weinheim, Germany).
2. Günes S, Neugebauer H, Sariciftci NS (2007) Conjugated polymer-based organic solar cells. *Chem Rev* 107:1324–1338.
3. Thompson BC, Fréchet JMJ (2008) Polymer–fullerene composite solar cells. *Angew Chem Int Ed* 47:58–77.
4. Pisula W, et al. (2006) Pronounced supramolecular order in discotic donor–acceptor mixtures. *Angew Chem Int Ed* 45:819–823.
5. Halls JJM, et al. (1995) Efficient photodiodes from interpenetrating networks. *Nature* 376:498–500.
6. Yu G, Gao J, Hummelen JC, Wudl F, Heeger AJ (1995) Polymer photovoltaic cells: Enhanced efficiencies via a network of internal donor-acceptor heterojunctions. *Science* 270:1789–1791.
7. Peumans P, Uchida S. Forrest SR (2003) Efficient bulk heterojunction photovoltaic cells using small molecular-weight organic thin films. *Nature* 425:158–162.
8. Li G, et al. (2005) High-efficiency solution processable polymer photovoltaic cells by self-organization of polymer blends. *Nat Mater* 4:864–868.
9. Kim JY, et al. (2007) Efficient tandem polymer solar cells fabricated by all-solution processing. *Science* 317:222–225.
10. Hoeben FJM, Jonkheijm P, Meijer EW, Schenning APHJ (2005) About supramolecular assemblies of π-conjugated systems. *Chem Rev* 105:1491–1546.
11. Würthner F, et al. (2004) Supramolecular p-n-heterojunctions by co-self-organization of oligo(*p*-phenylene vinylene) and perylene bisimide dyes. *J Am Chem Soc* 126:10611–10618.
12. Li WS, et al. (2008) Amphiphilic molecular design as a rational strategy for tailoring bicontinuous electron donor and acceptor arrays: Photoconductive liquid crystalline oligothiophene-C_{60} dyads. *J Am Chem Soc* 130:8886–8887.
13. Sisson AL, et al. (2008) Zipper assembly of vectorial rigid-rod π-stack architectures with red and blue naphthalenediimides: Toward supramolecular cascade n/p-heterojunction. *Angew Chem Int Ed* 47:3727–3729.
14. Kira A, et al. (2009) Supramolecular donor–acceptor heterojunctions by vectorial stepwise assembly of porphyrins and coordination-bonded fullerene arrays for photocurrent generation. *J Am Chem Soc* 131:3198–3200.
15. Yamamoto Y, et al. (2006) Photoconductive coaxial nanotubes of molecularly connected electron donor and acceptor layers. *Science* 314:1761–1764.
16. Watson MD, Fechtenkötter A, Müllen K (2001) Big is beautiful–''aromaticity'' revisited from the viewpoint of macromolecular and supramolecular benzene chemistry. *Chem Rev* 101:1267–1300.
17. Wu J, Pisula W, Müllen K (2007) Graphenes as potential material for electronics. *Chem Rev* 107:718–747.
18. Hill JP, et al. (2004) Self-assembled hexa-*peri*-hexabenzocoronene graphitic nanotube. *Science* 304:1481–1484.
19. Jin W, et al. (2005) Self-assembled graphitic nanotubes with one-handed helical arrays of a chiral amphiphilic molecular graphene. *Proc Natl Acad Sci USA* 102:10801–10805.
20. Jin W, et al. (2008) Systematic studies on structural parameters for nanotubular assembly of hexa-*peri*-hexabenzocoronenes. *J Am Chem Soc* 130:9434–9440.
21. Jin W, et al. (2005) Controlled self-assembly triggered by olefin metathesis: Cross-linked graphitic nanotubes from an amphiphilic hexa-*peri*-hexabenzocoronene. *J Am Chem Soc* 127:8284–8285.
22. Motoyanagi J, Fukushima T, Kosaka A, Ishii N, Aida T (2006) Self-assembled graphitic nanotubes from an amphiphilic hexabenzocoronene bearing thiol functionalities: Redox-mediated polymerization and depolymerization. *J Polymer Sci A* 44:5120–5127.
23. Mynar JL, et al. (2008) Radially diblock nanotube: Site-selective functionalization of a tubularly assembled hexabenzocoronene. *J Am Chem Soc* 130:1530–1531.
24. Motoyanagi J, Fukushima T, Ishii N, Aida T (2006) Photochemical stitching of a tubularly assembled hexabenzocoronene amphiphile by dimerization of coumarin pendants. *J Am Chem Soc* 128:4220–4221.
25. Yamamoto Y, et al. (2007) Molecular engineering of coaxial donor–acceptor heterojunction by coassembly of two different hexabenzocoronenes: Graphitic nanotubes with enhanced photoconducting properties. *J Am Chem Soc* 129:9276–9277.
26. Zhang G, et al. (2007) Formation of water-dispersible nanotubular assembly decorated with isothiouronium ion groups and its supramolecular functionalization. *J Am Chem Soc* 129:719–722.
27. Yamamoto T, et al. (2006) Stabilization of a kinetically favored nanostructure: Surface ROMP of self-assembled conductive nanocoils from a norbornene-appended hexa-*peri*-hexabenzocoronene. *J Am Chem Soc* 128:14337–14340.
28. Yamamoto T, et al. (2008) Conductive one-handed nanocoils by coassembly of hexabenzocoronenes: Control of morphology and helical chirality. *Angew Chem Int Ed* 47:1672–1675.
29. Yamamoto Y, et al. (2006) A glass hook allows fishing of hexa-*peri*-hexabenzocoronene graphitic nanotubes: Fabrication of a macroscopic fiber with anisotropic electrical conduction. *Adv Mater* 18:1297–1300.
30. Haddon RC, Perel AS, Morris RC, Palstra TTM, Hebard AF (1995) C_{60} thin film transistors. *Appl Phys Lett* 67:121–123.
31. Zaumseil J, Sirringhaus H (2007) Electron and ambipolar transport in organic field-effect transistors. *Chem Rev* 107:1296–1323.
32. Saeki A, Seki S, Takenobu T, Iwasa Y, Tagawa S (2008) Mobility and dynamics of charge carriers in rubrene single crystals studied by flash-photolysis microwave conductivity and optical spectroscopy. *Adv Mater* 20:920–923.
33. Amaya T, et al. (2009) Anisotropic electron transport properties in sumanene crystal. *J Am Chem Soc* 131:408–409.
34. van de Craats AM, et al. (1999) Record charge carrier mobility in a room-temperature discotic liquid-crystalline derivative of hexabenzocoronene. *Adv Mater* 11:1469–1472.
35. Dresselhaus MS, Dresselhaus G (1981) Intercalation compounds of graphite. *Adv Phys* 30:139–326.